Inelastic light scattering by intrasubband spin-density excitations in GaAs-AlGaAs quantum wells with balanced Bychkov-Rashba and Dresselhaus spin-orbit interaction: Quantitative determination of the spin-orbit field

S. Gelfert,[1] C. Frankerl,[1] C. Reichl,[2] D. Schuh,[1] G. Salis,[3] W. Wegscheider,[2] D. Bougeard,[1] T. Korn,[4] and C. Schüller[1,*]

[1]*Institut für Experimentelle und Angewandte Physik, Universität Regensburg, D-93040 Regensburg, Germany*
[2]*Solid State Physics Laboratory, ETH Zurich, 8093 Zurich, Switzerland*
[3]*IBM Research-Zurich, 8803 Rüschlikon, Switzerland*
[4]*Institut für Physik, Universität Rostock, D-18059 Rostock, Germany*

Inelastic light scattering experiments on low-energy intrasubband spin-density excitations (SDEs) are performed in (001)-grown modulation-doped GaAs-AlGaAs single quantum wells in in-plane external magnetic fields. The investigated samples possess balanced linear Bychkov-Rashba (α) and Dresselhaus (β) spin-orbit strengths in two different configurations, $\alpha = \beta$ and $\alpha = -\beta$. Both configurations lead to an extreme anisotropy of the spin splitting of the conduction band, where the in-plane directions of maximum spin splitting for both configurations are perpendicular to each other. The spin splitting asymmetry can be directly detected via the SDE by breaking of the time-reversal symmetry due to transfer of a momentum **q** in the quantum-well plane. In addition, the application of an in-plane magnetic field $\mathbf{B}_{\text{ext}} \perp \mathbf{q}$ allows us to modulate the effective magnetic field. Via a numerical line-shape analysis of the experimental SDE spectra, we determine the relevant parameters of the samples. We find that the linear spin-orbit strength $|\alpha| = \beta$ is comparable for both samples, while the electron g factors are markedly different. Furthermore, we experimentally quantify the values of the maximum internal spin-orbit fields, which are as high as $B_{\text{so}} \sim 18\,\text{T}$ for both samples.

I. INTRODUCTION

Resonant inelastic light scattering (RILS) is a very powerful tool for the investigation of electronic excitations in semiconductor nanostructures. In fact, more than two decades ago, the first experimental proof of the interplay of the so-called Bychkov-Rashba [1] and Dresselhaus [2] spin-orbit interaction in two-dimensional electron systems (2DES) in GaAs-AlGaAs quantum wells was made by RILS in the pioneering experiments of Jusserand and Richards *et al.* [3–6]. The collective electronic excitations in such systems are coherent density oscillations of the 2DES, either oscillations of the charge density, so-called charge-density excitations (CDE), or oscillations of the spin density, so-called spin-density excitations (SDE). Due to direct Coulomb interaction, the CDEs are typically blue-shifted with respect to the corresponding SDEs [7]. The electronic excitations can either be excitations between different subbands of the 2DES (intersubband excitations), or excitations within a subband (intrasubband excitations). In crystals with zinc blende structure, CDEs and SDEs can be separated in RILS experiments by polarization selection rules [8]: CDEs are visible for parallel polarizations of the incoming and scattered light, while SDEs require perpendicular linear polarizations. Under conditions of extreme resonance, also excitations which show characteristics of single-particle excitations (SPEs) can be

observed [9,10]. These excitations do not obey polarization selection rules. It is assumed that they are incoherent density oscillations with no fixed phase relation between individual electrons, and, hence, their energies are close to the excitation energies of noninteracting particles, i.e., they can be regarded as SPEs [11,12].

Typically, spin-orbit interaction in low-dimensional semiconductor systems has been considered as an effective, k-dependent spin-orbit field acting on individual electrons. Generally, for electrons in quantum wells with zinc blende lattice, the spin-orbit field consists of a Dresselhaus contribution with linear strength β, due to the bulk inversion asymmetry of the host crystal, and a Bychkov-Rashba term (with linear strength α), which is present if there is an asymmetry of the structure, caused by, e.g., external electric fields and/or space charges due to asymmetric modulation doping. The effect of this single-particle-like Bychkov-Rashba and Dresselhaus spin-orbit interaction on the propagation of intrasubband CDEs (plasmons) in quantum wells was theoretically considered by Badalyan *et al.* [13]. On the other hand, on the basis of RILS experiments on intersubband and intrasubband SDEs, it was suggested by Baboux *et al.* [14,15] that—due to collective effects—the spin-orbit field in the coherent SDEs may be enhanced by up to a factor of five [14], compared to the spin-orbit interaction of individual electrons, e.g., inside a spin packet. Furthermore, in Ref. [14] it was shown that the intersubband SDE, which microscopically is a triplet excitation with spin $S = 1$, splits in the collective spin-orbit field into three components with magnetic quantum numbers

*christian.schueller@ur.de

$m_S = 0, \pm 1$ if a finite wave vector **q** is transferred to the SDE, allowing a break of time-reversal symmetry. In this work we show that for intrasubband SDEs in two comparable GaAs-AlGaAs quantum-well structures, the sample parameters can be consistently described by the well-known Bychkov-Rashba and Dresselhaus spin-orbit terms. This may be due to the fact that the intrasubband SDEs are strongly Landau damped, and, hence, are dominantly of single-particle character. However, we observe significantly different g factors in our two samples, which may be taken as indicative of weak collective contributions to the SDEs.

Two-dimensional systems with balanced Rashba and Dresselhaus spin-orbit strength, i.e., $\alpha = \pm \beta$, have moved into the focus of spintronic research, motivated by a theoretical work of Schliemann *et al.* [16], who proposed a nonballistic spin field-effect transistor, and, later, of Bernevig *et al.* [17], where the authors proposed a new spin rotational SU(2) symmetry, which should lead to the formation of a persistent spin helix (PSH). The PSH was subsequently experimentally demonstrated by different groups [18–20]. In an earlier work, some of the authors and others have investigated the spin-orbit spin splitting of a 2DES with balanced Rashba and Dresselhaus spin-orbit strengths, $\alpha = \beta$, by RILS from the intrasubband SDE [21]. In these experiments, a wave vector **q** was either transferred parallel to the [110] in-plane direction of the GaAs-AlGaAs quantum well, where the two contributions of spin-orbit interaction add up, or parallel to [1$\bar{1}$0], where they cancel each other. Furthermore, in the presence of external magnetic fields, we could show that a superposition of the intrinsic spin-orbit field and the external magnetic field occurs [22].

In this work, we use RILS measurements to obtain further understanding of spin-orbit field parameters for samples with balanced Rashba and Dresselhaus spin-orbit contribution. In particular, we compare the two different configurations, $\alpha = \beta$ and $\alpha = -\beta$. By rotating the samples on a rotary stage, we precisely map the anisotropic spin splitting, and, depending on the configuration $\alpha = \beta$ (sample A) or $\alpha = -\beta$ (sample B), we show that the maximum spin splitting occurs parallel to [110] or parallel to [1$\bar{1}$0], respectively. Furthermore, by applying in-plane external magnetic fields, we directly determine the g factors of the samples and the absolute maximum strengths of the intrinsic spin-orbit fields. Surprisingly, the g factors turn out to be significantly different, though the nominal quantum-well widths and compositions are the same for both samples. On the other hand, the maximum spin-orbit field $\mathbf{B}_{so} \sim 18$ T is almost identical for both samples. It is governed by the relation $k_F / g(|\alpha| + \beta)$, with g the electron g factor and k_F the Fermi momentum. All extracted parameters can be consistently described and verified on a single-particle basis. Thus, we detect no significant influence of many-particle interaction on the strength of the spin-orbit field in SDEs, as was reported in Refs. [14,15]. However, we observe a $\sim 50\%$ difference in the g factors.

II. EXPERIMENTAL DETAILS

The two investigated samples were grown via molecular-beam epitaxy and contain (001)-oriented, n-modulation-doped GaAs-Al$_x$Ga$_{1-x}$As ($x = 0.30$ for sample A, $x = 0.33$
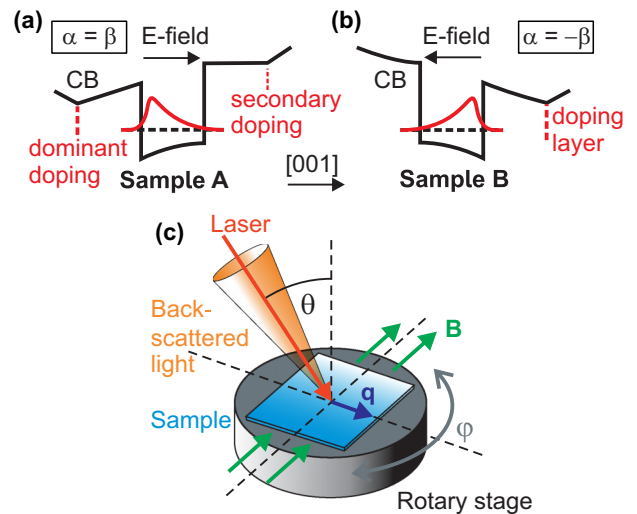

FIG. 1. (a) Asymmetric conduction-band profile of sample A. (b) Same for sample B. (c) Sketch of the experimental configuration for the RILS experiments (see text).

for sample B) single quantum wells with 12-nm well width. Their parameters were designed for equal strengths of the linear Rashba and Dresselhaus coefficients, α and β, respectively. Sample A is from the same wafer which was used in Refs. [19,21,22]. In Ref. [19], the PSH in this sample was imaged for the first time by direct spatial mapping, using time-resolved Kerr microscopy. The wafer was grown with a so-called inverted doping profile, where the dominant doping layer is grown before the quantum-well layer. This was done in order to induce an electric field across the quantum well in growth direction ([001] direction). Figure 1(a) is a schematic of the conduction-band potential profile of this sample. The space charges inside the quantum well and in the doping regions lead to an electric field in [001] direction [23]. The 2DES has an electron carrier density and mobility of $n \sim 5.0 \times 10^{15}$ m^{-2} and $\mu \sim 33$ m^2 V^{-1}s^{-1}, respectively, as determined from transport experiments [19]. From the line-shape analysis of our RILS experiments (see below), we determine a reduced carrier density of $n \sim (2.7 \pm 0.3) \times 10^{15}$ m^{-2}, which is on the one hand due to the redistribution of electrons from the quantum well to the ionized donors in the barriers via laser illumination. On the other hand, fluctuations in the donor distribution may contribute to this quite large difference since a different piece of the wafer was used. For our further analyses, we use this value of n, since it follows directly from the spectroscopic data. The effective mass of the electrons, $m^* \sim 0.075 m_0$, was determined from Raman experiments on cyclotron-resonance excitations in a perpendicular magnetic field (not shown). The measured effective mass is larger than the band-edge mass of GaAs, $m^* = 0.067 m_0$, for two reasons. (i) The first is the nonparabolicity of the conduction band: The electrons that contribute to the intraband and cyclotron-resonance excitations are close to the Fermi energy, which is about 10–20 meV above the conduction-band edge. (ii) The second is the penetration of the electron wave function into the barrier material (AlGaAs), which has a larger effective mass.

Sample B is n-modulation-doped only on the surface side of the quantum-well layer. So the built-in electric field points along the [00$\bar{1}$] direction, which leads to the configuration of $\alpha \sim -\beta$, with β being positive [23]. A sample of the same wafer was used in Ref. [24], where the existence of a PSH was shown via time-resolved Kerr microscopy. Figure 1(b) shows a schematic picture of the conduction-band profile of the quantum well in this sample. The 2DES of the sample has an electron density of $n \sim 5.9 \times 10^{15}$ m^{-2} and mobility of $\mu \sim 84$ m^2 V^{-1} s^{-1}, as determined from magneto-transport measurements. Again, from our spectroscopic data (see below) we extract a slightly lower electron density of $n \sim (5.8 \pm 0.7) \times 10^{15}$ m^{-2}. The effective electron mass of $m^* \sim 0.079 m_0$ was also determined from cyclotron resonance Raman experiments. The slightly larger effective mass of sample B, as compared to sample A, may be due to the larger carrier density in this sample and, hence, larger Fermi energy.

For the RILS experiments, a tunable continuous-wave Ti:Sapphire laser was used, which was tuned slightly above the band gap of the quantum well for near-resonant excitation. For the experiments presented in this manuscript, the samples were mounted in a He flow magnetocryostat at a nominal temperature of $T = 1.8$ K. However, from the line-shape analysis of our spectra we extract a temperature of the 2DES of about $T = 12$ K, which is due to heating of the 2DES by the incident laser. All experiments were performed in backscattering geometry. By tilting the sample normal with respect to the direction of the incoming and scattered light by an angle θ, a finite wave vector **q** can be transferred to the 2DES, as shown in Fig. 1(c). For this configuration, the wave-vector transfer q is given by $q \sim 4\pi/\lambda \sin\theta$, where λ is the wavelength of the laser light. Tilting angles of $\theta = 35°$ and $40°$ were used in our experiments. For the transfer of **q** into arbitrary in-plane crystal directions φ, the samples were mounted on an Attocube piezo-driven rotary stage with resistive position encoder. Optional in-plane external magnetic fields **B** with magnitudes of up to 6 T were generated by a superconducting split coil magnet. The direction of **q** with respect to **B** was fixed at 90° [see Fig. 1(c)]. The scattered light was analyzed in a triple Raman spectrometer and detected by a liquid-nitrogen-cooled charge-coupled-device camera. For all experiments, a depolarized scattering geometry was used, i.e., crossed linear polarizations of incident and scattered light in order to be sensitive for SDEs. The asymmetric line shapes of the experimental spectra were analyzed via a computational line-shape analysis, based on the Lindhard-Mermin line shape of intrasubband excitations [25,26].

III. THEORETICAL CONSIDERATIONS

The effect of relativistic spin-orbit interaction on an electron, moving in a periodic crystal potential, can be described in terms of an effective magnetic field **B**$_{so}$. For a superposition of the linear Bychkov-Rashba and the linear Dresselhaus contributions with strengths α and β, respectively, the intrinsic effective magnetic field in a (001)-grown quantum well is given by

$$\mathbf{B}_{so} = \frac{2}{g\mu_B}\{(\alpha k_y + \beta k_x)\mathbf{e}_x - (\alpha k_x + \beta k_y)\mathbf{e}_y\}. \quad (1)$$

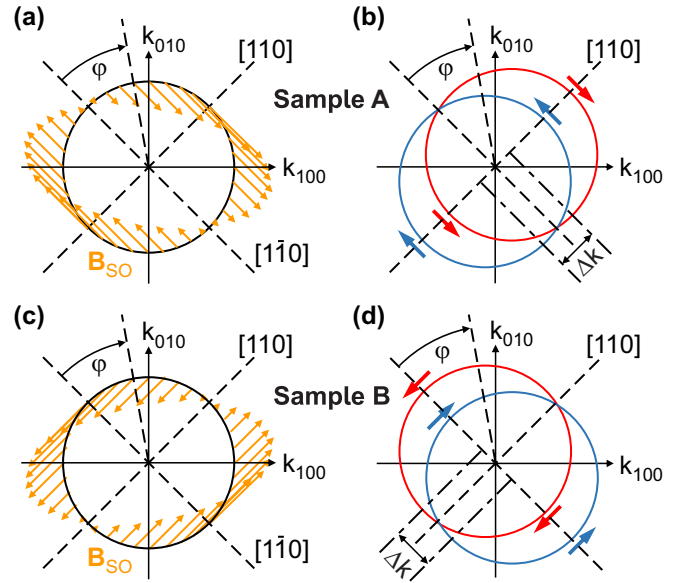FIG. 2. (a) Schematic picture of the unidirectional effective spin-orbit field **B**$_{so}$ of a 2DES with balanced Bychkov-Rashba and Dresselhaus spin-orbit strengths $\alpha = \beta$ (sample A). The angle φ is measured clockwise with respect to the [$\bar{1}$10] in-plane direction. (b) Fermi contour for spins parallel and antiparallel to **B**$_{so}$ for sample A. (c) Schematic picture of **B**$_{so}$ for sample B ($\alpha = -\beta$). (d) Fermi contour for sample B.

Here x, y, and z are parallel to the [100], [010], and [001] directions, respectively. g is the effective g factor and μ_B the Bohr magneton. For balanced Rashba and Dresselhaus interactions, $\alpha = \pm\beta$, Eq. (1) reduces to

$$\mathbf{B}_{so} = \frac{|\alpha| + \beta}{g\mu_B}(k_x \pm k_y)(\mathbf{e}_x \mp \mathbf{e}_y). \quad (2)$$

This situation is schematically displayed in Fig. 2(a) for $\alpha = \beta$: **B**$_{so}$ is either parallel or antiparallel to the [1$\bar{1}$0] in-plane direction, which leads to a spin splitting for in-plane spins, as schematically shown in Fig. 2(b) for the Fermi contour of the 2DES. The two energy paraboloids for spins parallel and antiparallel to [1$\bar{1}$0] are shifted in k space by a maximum value of Δk_{110} relative to each other. For arbitrary in-plane directions, denoted by the angle φ in Figs. 2(a) and 2(b), the magnitude of the shift of the two parabolas in this direction is given by

$$\Delta k_\varphi = \Delta k_{110}|\sin\varphi|. \quad (3)$$

For the situation $\alpha = -\beta$, the patterns in Figs. 2(a) and 2(b) are rotated clockwise by 90° and time reversed, i.e., **B**$_{so}$ is then parallel or antiparallel to the [110] in-plane direction [see Figs. 2(c) and 2(d)].

We turn now to the discussion of intrasubband SDEs, as investigated in this work via RILS. For simplicity, we discuss here explicitly the case $\alpha = \beta$ (sample A) only. The discussion for $\alpha = -\beta$ is exactly the same, except that $\varphi = 0°$ then has to be replaced by $\varphi = 90°$, because of the clockwise rotation of the relevant spin and field patterns. In the following, the terms "spin up" and "spin down" refer to the two different in-plane spin orientations [21]. In the backscattering
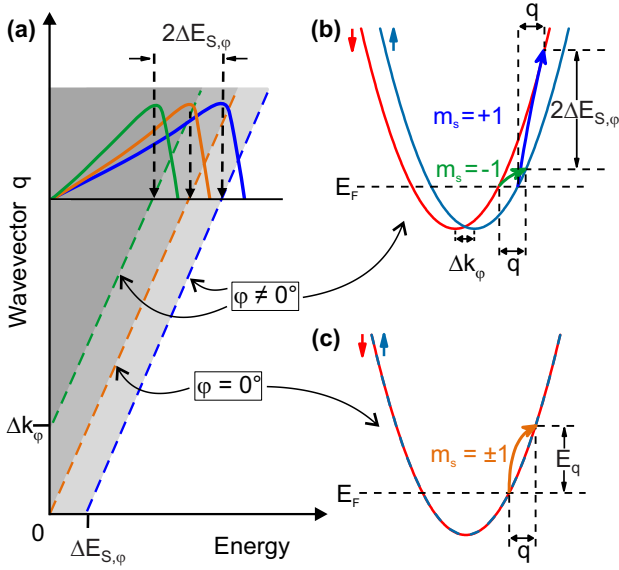
FIG. 3. (a) Single-particle continua for intrasubband spinflip excitations for in-plane directions of the wave-vector transfer q corresponding to $\varphi = 0°$ and $\varphi \neq 0°$, as valid for $\alpha = \beta$ (sample A). (b) Cut through the energy paraboloids [from Fig. 2(b)]: Spinflip transitions (arrows), which correspond to the high-energy cutoffs of the single-particle continua for $\varphi \neq 0°$. (c) Same as (b), for $\varphi = 0°$, where the spin splitting is zero.

geometry, only spinflip intrasubband transitions are allowed (cf. Ref. [21]), i.e., for the intrasubband SDE, spinflip transitions between states of different in-plane spin orientations have to be considered only. Consequently, this means that the SDE is a triplet excitation with magnetic quantum numbers $m_s = \pm 1$ only and $m_s = 0$ does not contribute [14]. In Fig. 3(a), the gray-shaded areas are displaying the single-particle continua for intrasubband spinflip excitations. For $\varphi = 0°$, the spin-up and spin-down states are degenerate [see Fig. 3(c)], i.e., the two excitations with $m_s = \pm 1$ are degenerate. The high-energy cutoff of the corresponding single-particle continuum for wave-vector transfer in this direction is given by $E_q = \frac{\hbar^2}{m^*} k_F q$, indicated by an orange dashed line in Fig. 3(a) [central dashed line in Fig. 3(a)]. For $\varphi \neq 0°$, the spinflip excitations with $m_s = +1$ and $m_s = -1$ are no longer degenerate, i.e., there are two spinflip transitions with different energies for a given wave-vector transfer q [see Fig. 3(b)] with high-energy cutoffs of $E_q^+ = \Delta E_{S,\varphi} + \frac{\hbar^2}{m^*} k_F q$, and $E_q^- = \frac{\hbar^2}{m^*} k_F (q - \Delta k_\varphi)$ [blue and green dashed lines in Fig. 3(a) and solid arrows in Fig. 3(b), i.e., right and left dashed lines in Fig. 3(a) and long and short curved arrows in Fig. 3(b)]. Here $\Delta E_{S,\varphi}$ is the maximum spin splitting at the Fermi level for in-plane direction φ. For a given wave-vector transfer q, the difference between E_q^+ and E_q^- is just twice the spin splitting, $E_q^+ - E_q^- = 2\Delta E_{S,\varphi}$ [see Fig. 3(b)], since

$$\Delta E_{S,\varphi} = \frac{\hbar^2}{m^*} k_F \Delta k_\varphi = 2(\alpha + \beta) k_F |\sin \varphi|. \quad (4)$$

For sample B, the right-hand side of Eq. (4) becomes

$$\Delta E_{S,\varphi} = 2(|\alpha| + \beta) k_F |\cos \varphi|. \quad (5)$$

In Fig. 3(a), the Lindhard-Mermin-type line shapes [25,26] of intrasubband spinflip excitations for a given q are schematically indicated as solid green, orange, and blue curves. In the underlying formalism, the excitation spectrum is calculated on the basis of single-particle transitions by evaluating the imaginary part of the dielectric response function $\chi_0(\omega, q, \tau)$ of a system of noninteracting particles and taking into account a finite single-particle scattering time τ and the temperature T. The four parameters, which determine the line shape, are the magnitude of the wave-vector transfer q, the electron density n, the electron temperature T, and the single-particle scattering time τ [26]. Since q is adjusted in the experiment and therefore known, there are only three free parameters. The maxima of the excitations are around the high-energy cutoffs of the corresponding single-particle continua, which are proportional to the Fermi wave vector k_F. Therefore, via the relation $k_F = \sqrt{2\pi n}$, the electron density n of the 2DES is determined very accurately by the energetic positions of the high-energy cutoffs of the spectra. As mentioned above, for in-plane spin orientations, only spinflip transitions of electrons are Raman allowed in depolarized scattering geometry, i.e., excitations with $m_s = \pm 1$. Therefore, for directions of the wave-vector transfer q with $\varphi \neq 0°$ (sample A) or $\varphi \neq 90°$ (sample B), we expect a superposition of the green and blue spectra of Fig. 3(a) (cf. Ref. [21]), corresponding to two maxima. By contrast for the particular cases of $\varphi = 0°$ (sample A) or $\varphi = 90°$ (sample B), i.e., $q \parallel [1\bar{1}0]$ or $q \parallel [110]$, respectively, there should be a single maximum, only [orange curve in Fig. 3(a)]. For the two extreme cases, $\varphi = 0°$ and $90°$, this was experimentally confirmed in Ref. [21] for sample A.

So far, we have discussed the intrasubband SDE in terms of single-particle spinflip excitations. It is well known that the intrasubband SDE is a collective excitation of the 2DES due to exchange Coulomb interaction. However, since the exchange interaction leads to a redshift of the collective SDE [9], its energy lies within the single-particle continua, which are displayed in Fig. 3(a). Hence, the collective SDE is strongly Landau damped due to the decay into uncorrelated spinflip excitations of individual electrons. For this reason, the collective shift of this excitation due to exchange interaction is known to be rather small [27]. It can be deduced from the comparison of RILS spectra in polarized geometry (see Supplemental Material [28]), where intrasubband nonspinflip single-particle excitations can be observed, with spectra measured in depolarized geometry, where the intrasubband SDE is visible [27].

IV. EXPERIMENTS AND RESULTS

With these considerations we are now ready to discuss the first set of experiments. Figure 4(a) shows a waterfall plot of depolarized RILS spectra of sample A for a tilt angle of $\theta = 35°$, i.e., a fixed wave-vector transfer of $q = 9.1 \times 10^6$ m^{-1}. Then, via the rotary stage, the sample is rotated in steps of $15°$ between positions $\varphi = 0°$ and $\varphi = 360°$. For each position, a RILS spectrum of the low-energy SDE is taken. The normalized spectra are displayed with vertical offsets for better comparison in Fig. 4(a). The gray shaded area indicates the cutoff of the triple Raman spectrometer. The evolution of the spectra from a Lindhard-Mermin spectrum at $\varphi = 0°$
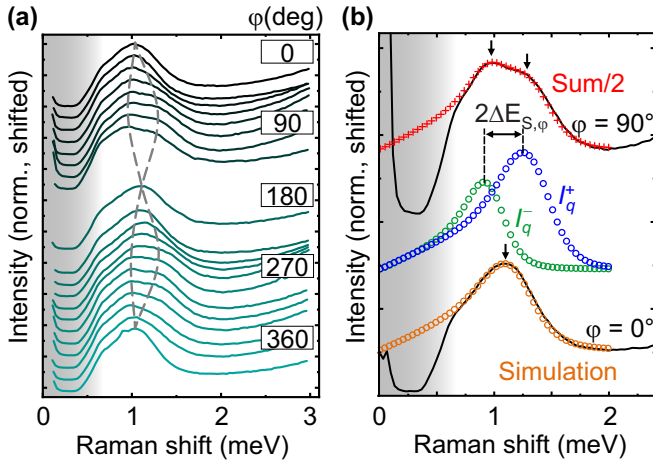
FIG. 4. (a) Waterfall plot of depolarized RILS spectra of sample A at a tilt angle of $\theta = 35°$, corresponding to a wave-vector transfer of $q = 9.1 \times 10^6$ m^{-1} for different in-plane directions φ (relative to [$\bar{1}$10]) at zero external magnetic field. The gray shaded area marks the spectrometer cutoff. The positions of the maxima are traced by the gray dashed lines. (b) Lindhard-Mermin line-shape analysis of measured spectra (black solid lines) exemplarily for minimum spin splitting at $\varphi = 0°$ (bottom spectrum) and maximum spin splitting at $\varphi = 90°$ (top spectrum).

FIG. 5. (a) Polar plot of extracted peak splittings versus angle φ (relative to [$\bar{1}$10] in-plane direction) for sample A at zero external magnetic field (inner open circles) and for external in-plane magnetic fields of 6 T (outer solid circles). The gray lines show the calculated $\sin\varphi$ dependence of the peak splitting. (b) Same as (a) but for sample B at a tilt angle of $\theta = 40°$, corresponding to a wave-vector transfer of $q = 10.2 \times 10^6$ m^{-1}. The increased peak splitting is due to the higher electron density of this sample.

to a superposition of two spectra with two different maxima (indicated by gray dashed lines) can clearly be recognized. When rotating φ by 360°, a periodic pattern for the shift of the maxima can be found, which resembles the expected spin splitting due to the effective spin-orbit field, shown in Fig. 2(b). To accurately extract the positions of the maxima in the spectra, i.e., the cutoff energies of the spinflip transitions, all measured spectra were reproduced via a computational line-shape analysis implemented in Python, based on the Lindhard-Mermin line shape [25,26], where $\chi_0(\omega, q, \tau)$ is calculated [8,29] by numerically integrating over all possible spinflip single-particle transitions in k space.

Our line-shape analysis procedure is exemplarily shown in Fig. 4(b) for the two extreme cases $\varphi = 0°$ and $\varphi = 90°$ for sample A. For $\varphi = 0°$ the measured single-peak spectrum (black solid line) in the lower part of Fig. 4(b) can nicely be reproduced by the simulation (orange open dots), using the following material parameters: Electron temperature of $T = 12$ K, single-particle scattering time of $\tau = 3$ ps and electron density of $n = (2.7 \pm 0.3) \times 10^{15}$ m^{-2}. We assume that the short lifetime of 3 ps is due to the strong Landau damping of the intrasubband SDE, since its energy is inside the single-particle continuum. The smaller electron density here, as compared to the transport measurements from Ref. [19], may arise from the strong laser illumination in our experiments. The experimental spectrum for $\varphi = 90°$ [solid black line in the upper part of 4(b)] is nicely reproduced by the superposition of two simulated curves I_q^+ and I_q^- [green and blue open dots in Fig. 4(b)], which are obtained by varying Δk_φ [see Eqs. (3) and (4)] until the simulation matches the measured spectra [red crosses in Fig. 4(b)]. The extracted peak splittings are just twice the spin splitting, $\Delta E_{S,\varphi}$, for the corresponding in-plane direction, as explained in the considerations above.
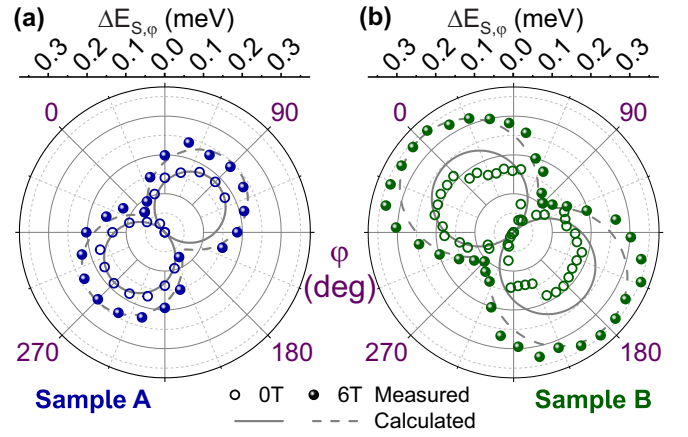
The results of this analysis for sample A, i.e., for the condition $\alpha = \beta$, are summarized in Fig. 5(a). The inner open symbols in Fig. 5(a) are showing the spin splittings $\Delta E_{S,\varphi}$ versus the angle φ (relative to [$\bar{1}$10] in-plane direction), derived via the above discussed line-shape analysis procedure for all measured spectra at zero external magnetic field. At $\varphi = 90°$ and 270° a maximum splitting of $\Delta E_S = (0.19 \pm 0.01)$ meV can be extracted for sample A, whereas for $\varphi = 0°$ and 180° no spin splitting is observable (cf. Ref. [21]). The solid gray line shows the computed values for the spin splitting, based on the above discussed $\sin\varphi$ dependence [see Eq. (3)]. For the intrinsic spin-orbit parameters α and β [after Eq. (4)], we receive for $(\alpha + \beta)/2 = \alpha = \beta = (3.50 \pm 0.25)$ meVÅ the best agreement with the experimental data, when using $n = 2.7 \times 10^{15}$ m^{-2} for the 2DES density, as determined from the line-shape analysis (see above). The parameters α and β, as deduced from the experiments in Ref. [19] on a different piece of the same wafer, are somewhat smaller. Those experiments were conducted at a higher temperature of $T = 40$ K. Additionally, in Ref. [19] a transient in Δk due to a finite excitation spot size [30] has not been included in the analysis. Similarly, the RILS experiments in Ref. [21] delivered slightly smaller values for α and β. In these experiments, a different laser excitation energy was used, leading to different resonance conditions and, hence, a different electron density in the optical experiment, corresponding to a different electric field across the quantum well.

Next we discuss the experiments in external magnetic fields. As indicated in Fig. 1(c), the externally applied field $\mathbf{B}_{ext}$ lies in-plane with the effective spin orbit field $\mathbf{B}_{so}$ [Figs. 2(a) and 2(c)] and, for each position of φ, perpendicular to the transferred wave vector ($\mathbf{B}_{ext} \perp \mathbf{q}$). This generally leads to a disturbance of the unidirectionality of the effective magnetic field acting on an electron, since the intrinsic and the external fields superimpose. The above described

measurement series, i.e., recording depolarized RILS spectra of the intrasubband SDE, while rotating the sample stepwise with respect to the fixed direction of **q**, is repeated for both samples with a fixed external magnetic field of $B_{ext} = 6$ T, and $\mathbf{B}_{ext} \perp \mathbf{q}$. The blue solid dots in Fig. 5(a) display the extracted spin splittings for sample A. A global increase of the spin splittings can be found with maxima $\Delta E_S = (0.24 \pm 0.01)$ meV at $\varphi = 90°$ and $270°$, where the external magnetic field $\mathbf{B}_{ext}$ is oriented parallel to the intrinsic spin-orbit field $\mathbf{B}_{so}$ so that they add up. For the orthogonal in-plane axis along $\varphi = 0°$ and $180°$, a finite splitting of $\Delta E_S = 0.15$ meV appears. Because of the unidirectional character of $\mathbf{B}_{so}$, this splitting can only stem from the Zeeman splitting due to the applied external magnetic field $\mathbf{B}_{ext}$. The measured values of $\Delta E_{S,\varphi}$ are in good agreement with the computed values [gray dashed line in Fig. 5(a)], which were calculated via the relation $\Delta E_{S,B}(\varphi) = g\mu_B |\mathbf{B}_{tot}(\varphi)|$, where the superposition of $\mathbf{B}_{ext}$ and $\mathbf{B}_{so}$ leads to a total effective magnetic field $\mathbf{B}_{tot}$. Using a $|g|$ factor of 0.16 ± 0.04, and the same values for $\alpha = \beta$ and n as for the $B_{ext} = 0$ measurement analysis above, the computed values [dashed gray line in Fig. 5(a)] fit best with the measured spin splittings. This g factor, which would, according to Ref. [31], correspond to a symmetric GaAs quantum well with width of about 8 nm, will be discussed in more detail below.

We now turn to measurements on sample B with negative Bychkov-Rashba spin-orbit parameter $\alpha = -\beta$. The intrinsic spin-orbit field $\mathbf{B}_{so}$ is still unidirectional according to Eq. (2), but, compared to sample A, now parallel or antiparallel to the orthogonal in-plane direction. Figure 5(b) shows the spin splittings $\Delta E_{S,\varphi}$, as extracted from the line-shape analysis of depolarized RILS spectra, for zero external magnetic field (inner open dots) and for an external magnetic field of $B_{ext} = 6$ T (green solid dots). The maximum spin splitting now emerges for $\varphi = 0°$ and $180°$ with a magnitude of $\Delta E_S = (0.20 \pm 0.01)$ meV for zero external magnetic field and $\Delta E_S = (0.34 \pm 0.01)$ meV for $B_{ext} = 6$ T. From the Lindhard-Mermin line-shape analysis we obtain an electron temperature of $T = 12$ K, a single-particle scattering time of $\tau = 3$ ps and an electron density of $n = (5.8 \pm 0.7) \times 10^{15}$ m^{-2}. For the calculation of the spin splittings [gray solid and dashed lines in Fig. 5(b)], the density of the 2DES is kept fixed at $n = 5.8 \times 10^{15}$ m^{-2} (see above), and the spin-orbit parameters [see Eq. (5)] are chosen to be $\alpha = -\beta = (-3.25 \pm 0.25)$ meV Å. The measured data points for $B_{ext} = 0$ T in Fig. 5(b) show a deviation from the calculated values. This could be due to inhomogeneities of the donor distribution in the sample, resulting in an inhomogeneity of the electron density n: By rotating the sample during a φ series, the laser spot may vary locally on the sample surface if the rotation axis is not perfectly aligned to the laser-spot position. For $B_{ext} = 6$ T, the measured data points are much closer fitting to the calculated values. Compared to sample A, the enlarged spin splitting [solid gray line in Fig. 5(b)] can be explained by the higher electron density, which, due to the relation $k_F = \sqrt{2\pi n}$ and Eq. (4), leads to an increase of $\Delta E_{S,\varphi}$. From this measurement, an effective $|g|$ factor of 0.23 ± 0.07 can be determined for sample B. Surprisingly, this g factor is almost 50% larger than the above presented g factor for sample A. According to Ref. [31], it would correspond to a symmetric GaAs quantum well with a width of about 10 nm.

We note here that in our analysis we have assumed an isotropic in-plane g factor. Actually, for GaAs-AlGaAs quantum wells with an asymmetric quantum-well potential, the in-plane g factor should be anisotropic [32–35], and the strength of the anisotropy depends on the potential asymmetry. In Ref. [35], e.g., a difference of about 20% was detected for the two in-plane directions [110] and [1$\bar{1}$0] in a GaAs-AlGaAs heterojunction. However, within our experimental error margins, we cannot clearly resolve such an anisotropy (cf. Fig. 5). We will come back to this point in more detail below, in Sec. V.

Finally, we demonstrate how the intrinsic effective spin-orbit field $\mathbf{B}_{so}$ can be determined directly by superimposing an external magnetic field. In the above measurements, a fixed magnetic field was applied, and the sample was rotated in order to change the in-plane crystal directions with respect to the magnetic field. From the variation of the spin splittings, extracted from RILS spectra of intrasubband SDE, first, the spin-orbit parameters are determined from the measurements at $B_{ext} = 0$, and then the g factors are derived from experiments at $B_{ext} \neq 0$. As outlined above, this measurement procedure is prone to be influenced by inhomogeneities of the sample if the laser spot is not perfectly aligned with the rotation axis. The carrier densities are determined by the positions of the high-energy cutoffs of the spectra. In principle, we could now compute the maximum spin-orbit field with these parameters. For $\alpha = \pm \beta$, the energy paraboloids for spin up and spin down are shifted against each other in k space [see Figs. 2(b) and 2(d)] by a momentum $\Delta \mathbf{k}$ with magnitude

$$\Delta k = \frac{4m^*\alpha}{\hbar^2}. \tag{6}$$

Inserting this into Eq. (4), and assuming a Zeeman-type energy splitting $\Delta E_S = g\mu_B B_{so}$, one gets for the magnitude of the maximum intrinsic spin-orbit field

$$B_{so} = \frac{4\alpha k_F}{g\mu_B}. \tag{7}$$

Inserting the parameters, as extracted above from the measurements of samples A and B, into Eq. (7), we receive for sample A $B_{so} \sim (19.9 \pm 4.1)$ T and for sample B $B_{so} \sim (18.6 \pm 3.9)$ T. The uncertainties are quite large, due to the uncertainties in the contributing individual parameters. In the following we will verify these field values by a direct, more accurate measurement. In order to do so, we fix the direction of wave-vector transfer **q** in the directions of maximum spin splittings, i.e., the [110] direction for sample A and the [1$\bar{1}$0] direction for sample B. Since $\mathbf{B}_{ext} \perp \mathbf{q}$, the external field is then parallel or antiparallel to the maximum internal spin-orbit field $\mathbf{B}_{so}$ [36]. Then we record a series of RILS spectra of the SDE for different external fields, ranging from -6 T to $+6$ T. In doing so, the laser spot is kept fixed on the sample surface, which reduces the possible influence of inhomogeneities to a minimum. Figure 6(a) shows such a series of depolarized RILS spectra for different external magnetic fields of sample B, recorded with a wave-vector transfer along $\varphi = 0°$ (**q** || [1$\bar{1}$0]), where the maximum spin splitting appears. A linear convergence of the peak splittings from positive to negative external magnetic fields is clearly visible.
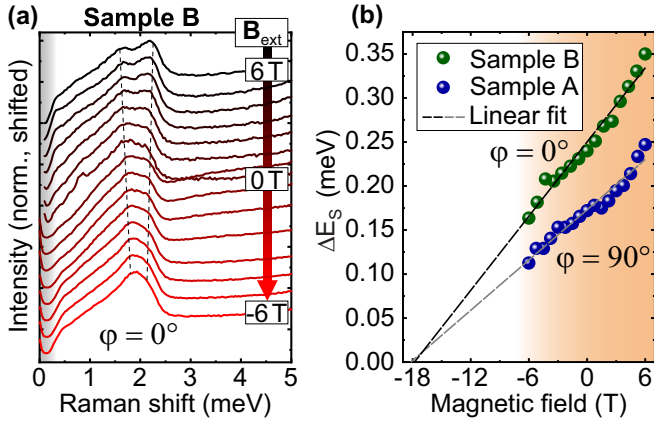
FIG. 6. (a) Depolarized RILS spectra of sample B for different external magnetic fields, oriented parallel for $B_{ext} > 0\ T$ and antiparallel for $B_{ext} < 0\ T$. The peaks are converging linearly due to a superposition of $\mathbf{B}_{ext}$ and $\mathbf{B}_{so}$. (b) Extracted spin splittings for both investigated samples, recorded with a wave-vector transfer along maximum spin splitting crystal direction. The orange shaded area is the experimentally accessible magnetic field range of the cryostat. Dashed line: Linear fit and extrapolation of the spin splittings.

We expect the effective spin-orbit field $\mathbf{B}_{tot}$ to be enhanced if the external magnetic field is oriented parallel to $\mathbf{B}_{so}$, which is the case for $B_{ext} > 0\ T$ and $\mathbf{B}_{tot}$ to be attenuated for antiparallel orientation, i.e., $B_{ext} < 0\ T$. The values for the splitting were extracted via the Lindhard-Mermin line-shape analysis and plotted against the external magnetic field in Fig. 6(b) for both investigated samples. For both samples a linear shift of the peak splitting occurs in the orange shaded area of Fig. 6(b), which marks the accessible magnetic field range of the cryostat. In particular, this measurement series shows a clear difference of the spin splitting of both samples for $B_{ext} = 0$. The value of this splitting for sample B nicely agrees with the calculated value in Fig. 5(b) for 0° and 180° [solid gray line in Fig. 5(b)], confirming the above-derived values for α and β. As discussed above, the corresponding experimental data in this figure [open green dots in Fig. 5(b)] may have been influenced by sample inhomogeneities. The strength of the intrinsic spin-orbit field $\mathbf{B}_{so}$ can be extracted by extrapolating the spin splittings (dashed lines) until their intersection with the x axis. For both samples we extract a value of $\sim(18 \pm 1)$ T, in good agreement with the computed values above. From the slope of the dashed lines we extract an effective $|g|$ factor of 0.17 ± 0.01 for sample A and 0.24 ± 0.01 for sample B, in almost perfect agreement with the values we have received from the angular-resolved measurements with fixed magnetic field [dashed gray lines in Figs. 5(a) and 5(b)].

V. DISCUSSION

We have investigated two single quantum-well samples with nominally identical GaAs wells of 12-nm width but opposite doping profiles, leading to oppositely oriented electric fields in the quantum well and, hence, linear Bychkov-Rashba parameters, α, with opposite sign. The electron densities n of the samples can be relatively accurately determined from

the high-energy cutoffs of the intrasubband SDE spectra via a Lindhard-Mermin line-shape analysis. This delivers different values for the two samples, namely $n \sim (2.7 \pm 0.3) \times 10^{15}\ \text{m}^{-2}$ for sample A and $n \sim (5.8 \pm 0.7) \times 10^{15}\ \text{m}^{-2}$ for sample B. Furthermore, from the line-shape analysis of the peak splittings at $B_{ext} = 0$, comparable magnitudes of the spin-orbit parameters $(|\alpha| + \beta)/2 = (3.50 \pm 0.25)$ meV Å for sample A and $(|\alpha| + \beta)/2 = (3.25 \pm 0.25)$ meV Å for sample B can be determined within the error bars. These values are consistently confirmed by the high accuracy measurements, displayed in Fig. 6, where the laser spot is kept at a fixed position on the sample surface. We believe that the approximate equivalence of the spin-orbit parameters in both samples is just by coincidence. It seems that the different doping profiles in the two samples [see Figs. 1(a) and 1(b)] result in approximately the same magnitude of the Bychkov-Rashba coefficient $|\alpha|$ for both samples. The g factors, extracted from the experiments in Fig. 6 with $B_{ext} \neq 0$ are, however, puzzling. It is obvious from Fig. 6 that the g factors for samples A and B are distinctly different. Puzzling is the fact that sample B, which has the larger electron density n, shows a g factor of $|g| = 0.24 \pm 0.01$, which is almost 50% larger than the g factor of sample A. This is counterintuitive: Assuming a negative g factor (as expected for a well width of 12 nm [37,38]), $|g|$ should decrease with increasing Fermi energy (and same well width). This is further corroborated by the fact that the effective mass, m^*, follows the expectation: It is slightly larger in sample B, which has the larger Fermi energy. This is expected because of the nonparabolicity of the conduction band of GaAs.

At a first glance, one could think that the difference in g factors for the two samples could be due to the anisotropy of the in-plane g factor [32,34,35]: The directions of maximum spin splitting in samples A and B are the [110] and the [$1\bar{1}0$] directions, respectively (cf. Fig. 5). In Ref. [35], these directions were experimentally found to be the directions of maximum anisotropy in a GaAs-AlGaAs heterojunction. However, due to the reversed electric fields in the two samples, the in-plane directions of maximum and minimum g factors are expected to switch between the two samples. As a result, in both samples the directions of maximum spin splitting correspond to the directions of maximum g factor. This can be proven as follows: A theoretical treatment yields for the nondiagonal elements of the in-plane g tensor [32,34]

$$g_{xy} = g_{yx} = \frac{2\gamma e}{\hbar^3 \mu_B}\left(\langle p_z^2\rangle\langle z\rangle - \langle p_z^2 z\rangle\right), \tag{8}$$

with the bulk Dresselhaus coefficient γ [2] and $\langle\rangle$ denoting the expectation value for the electron wave function. The two terms in the brackets on the right-hand side of Eq. (8) exactly cancel if the quantum-well potential is symmetric, i.e., then the in-plane g factor is isotropic. The larger the asymmetry of the potential, the larger is the magnitude of the offdiagonal element g_{xy}. With Eq. (8) and the electronic wave functions of samples A and B [cf., Figs. 1(a) and 1(b)] it follows that $g_{xy} > 0$ for sample A and $g_{xy} < 0$ for sample B, provided that $\gamma > 0$. For a small magnetic field $\mathbf{B}_{ext}$, pointing in an arbitrary in-plane direction φ, as defined above, the anisotropic $g(\varphi)$ is

given by [34]

$$g(\varphi) = -\sqrt{g_{xx}^2 + g_{xy}^2 + 2g_{xx}g_{xy}\cos(2\varphi)}. \tag{9}$$

We have to take into account now that in our experiments we have $\mathbf{B}_{\text{ext}} \perp \mathbf{q}$. This means that, e.g., in an experiment on sample A with $\mathbf{q} \parallel [110]$, i.e., in direction of maximum spin splitting, $\mathbf{B}_{\text{ext}} \parallel [1\bar{1}0]$, and so on. Altogether, employing Eq. (9), this results in the relations $|g_{110}| = |g(180°)| > |g_{1\bar{1}0}| = |g(-90°)|$ for sample A and $|g_{1\bar{1}0}| = |g(-90°)| > |g_{110}| = |g(180°)|$ for sample B. This confirms the above statement that the directions of maximum spin splitting in both samples ([110] for sample A and [1$\bar{1}$0] for sample B) are the directions of maximum in-plane g factor. Hence, the quite significant difference of the measured g factors cannot be explained by the g factor anisotropy.

We speculate that the difference in g factors is due to residual collective effects in the Landau-damped SDE, which may lead to an enhanced spin-orbit field and, hence, an enlarged splitting. If we rewrite Eq. (4) for the situation when the external field is parallel to the intrinsic spin-orbit field [as in the experiments, displayed in Fig. 6] for a Zeeman-like energy splitting, then we have for the spin splitting

$$\Delta E_{S,\text{max}} = 2(|\alpha| + \beta)k_F + g\mu_B B_{\text{ext}} = g\mu_B[B_{\text{so}} + B_{\text{ext}}]. \tag{10}$$

Equation (10) may contain g as an effective g factor, modeling the effect of a collective spin-orbit field. However, at the moment it is not clear whether it is just an enhancement of the g factor due to many-particle interaction or an enhanced spin-orbit field. This is so far a naive assumption and further theoretical elaboration is needed for an accurate description of the relevant effects.

Finally, we note that having approximately the same magnitude of the spin-orbit field B_{so} in both samples, e.g., on the basis of Eq. (7) means that the relation k_F/g in both samples has to be the same. This would mean that a larger k_F (sample B) is compensated for by a larger g factor and vice versa for sample A. For our extracted parameters, this is the case (see above). The conclusion regarding whether this is significant or just coincidence for the two investigated samples will need more investigations from the experimental as well as theoretical sides.

VI. CONCLUSION

In conclusion, we compared two samples possessing balanced Bychkov-Rashba and Dresselhaus spin-orbit coupling but with different sign of the Rashba parameter, i.e., $\alpha = \pm\beta$, by their spectra of intrasubband SDEs. For each sample, we precisely mapped the spin splitting of the 2DES and could show that the unidirectional spin-orbit field is pointing parallel and antiparallel along the [1$\bar{1}$0] in-plane direction for $\alpha = \beta$ and along [110] for $\alpha = -\beta$. With in-plane external magnetic fields, we were able to deduce the strengths of the maximum intrinsic spin-orbit fields. We found an effective g factor, which is significantly enhanced for the sample with the larger density, possibly indicating the influence of collective effects in the intrasubband SDEs.

[1] Y. A. Bychkov and E. I. Rashba, Pisma Zh. Eksp. Teor. Fiz. **39**, 66 (1984); JETP Lett. **39**, 78 (1984).

[2] G. Dresselhaus, Phys. Rev. **100**, 580 (1955).

[3] B. Jusserand, D. Richards, H. Peric, and B. Etienne, Phys. Rev. Lett. **69**, 848 (1992).

[4] D. Richards, B. Jusserand, H. Peric, and B. Etienne, Phys. Rev. B **47**, 16028 (1993).

[5] B. Jusserand, D. Richards, G. Allan, C. Priester, and B. Etienne, Phys. Rev. B **51**, 4707 (1995).

[6] D. Richards, B. Jusserand, G. Allan, C. Priester, and B. Etienne, Solid-State Electron. **40**, 127 (1996).

[7] A. Pinczuk and G. Abstreiter, *Light Scattering in Solids V*, edited by M. Cardona and G. Güntherodt (Springer, Heidelberg, 1988).

[8] D. C. Hamilton and A. L. McWhorter, *Light Scattering Spectra of Solids*, edited by G. B. Wright (Springer, New York, 1969).

[9] A. Pinczuk, S. Schmitt-Rink, G. Danan, J. P. Valladares, L. N. Pfeiffer, and K. W. West, Phys. Rev. Lett. **63**, 1633 (1989).

[10] C. Schüller, G. Biese, K. Keller, C. Steinebach, D. Heitmann, P. Grambow, and K. Eberl, Phys. Rev. B **54**, R17304 (1996).

[11] C. Steinebach, C. Schüller, and D. Heitmann, Phys. Rev. B **59**, 10240 (1999).

[12] C. Steinebach, C. Schüller, and D. Heitmann, Phys. Rev. B **61**, 15600 (2000).

[13] S. M. Badalyan, A. Matos-Abiague, G. Vignale, and J. Fabian, Phys. Rev. B **79**, 205305 (2009).

[14] F. Baboux, F. Perez, C. A. Ullrich, I. D'Amico, J. Gómez, and M. Bernard, Phys. Rev. Lett. **109**, 166401 (2012).

[15] F. Baboux, F. Perez, C. A. Ullrich, I. D'Amico, G. Karczewski, and T. Wojtowicz, Phys. Rev. B **87**, 121303(R) (2013).

[16] J. Schliemann, J. C. Egues, and D. Loss, Phys. Rev. Lett. **90**, 146801 (2003).

[17] B. A. Bernevig, J. Orenstein, and S.-C. Zhang, Phys. Rev. Lett. **97**, 236601 (2006).

[18] J. D. Koralek, C. P. Weber, J. Orenstein, B. A. Bernevig, S.-C. Zhang, S. Mack, and D. D. Awschalom, Nature **458**, 610 (2009).

[19] M. P. Walser, C. Reichl, W. Wegscheider, and G. Salis, Nat. Phys. **8**, 757 (2012).

[20] M. Kohda, V. Lechner, Y. Kunihashi, T. Dollinger, P. Olbrich, C. Schönhuber, I. Caspers, V. V. Bel'kov, L. E. Golub, D. Weiss, K. Richter, J. Nitta, and S. D. Ganichev, Phys. Rev. B **86**, 081306(R) (2012).

[21] C. Schönhuber, M. P. Walser, G. Salis, C. Reichl, W. Wegscheider, T. Korn, and C. Schüller, Phys. Rev. B **89**, 085406 (2014).

[22] S. Gelfert, C. Frankerl, C. Reichl, D. Schuh, G. Salis, W. Wegscheider, D. Bougeard, T. Korn, and C. Schüller, Spintronics XI, Proc. SPIE **10732**, 1073219 (2018).

[23] M. Studer, G. Salis, K. Ensslin, D. C. Driscoll, and A. C. Gossard, Phys. Rev. Lett. **103**, 027201 (2009).

[24] M. Schwemmer, A. Hanninger, M. Weingartner, M. Oltscher, M. Ciorga, D. Weiss, D. Schuh, D. Bougeard, T. Korn, and C. Schüller, Appl. Phys. Lett. **109**, 172106 (2016).

[25] N. D. Mermin, Phys. Rev. B **1**, 2362 (1970).

[26] G. Fasol, N. Mestres, A. Fischer, and K. Ploog, Phys. Scr. **T19A**, 109 (1987).

[27] M. Berz, J. F. Walker, P. von Allmen, E. F. Steigmeier, and F. K. Reinhart, Phys. Rev. B **42**, 11957 (1990).

[28] See Supplemental Material at http://link.aps.org/supplemental/10.1103/PhysRevB.101.035427 for a comparison of polarized and depolarized RILS spectra.

[29] F. Stern, Phys. Rev. Lett. **18**, 546 (1967).

[30] G. Salis, M. P. Walser, P. Altmann, C. Reichl, and W. Wegscheider, Phys. Rev. B **89**, 045304 (2014).

[31] I. A. Yugova, A. Greilich, D. R. Yakovlev, A. A. Kiselev, M. Bayer, V. V. Petrov, Y. K. Dolgikh, D. Reuter, and A. D. Wieck, Phys. Rev. B **75**, 245302 (2007).

[32] V. K. Kalevich and V. L. Korenev, Pis'ma Zh. Eksp. Teor. Fiz. **57**, 557 (1993); JETP Lett. **57**, 571 (1993).

[33] G. Salis, D. D. Awschalom, Y. Ohno, and H. Ohno, Phys. Rev. B **64**, 195304 (2001).

[34] P. S. Eldridge, J. Hübner, S. Oertel, R. T. Harley, M. Henini, and M. Oestreich, Phys. Rev. B **83**, 041301(R) (2011).

[35] Y. A. Nefyodov, A. V. Shchepetilnikov, I. V. Kukushkin, W. Dietsche, and S. Schmult, Phys. Rev. B **84**, 233302 (2011).

[36] M. P. Walser, U. Siegenthaler, V. Lechner, D. Schuh, S. D. Ganichev, W. Wegscheider, and G. Salis, Phys. Rev. B **86**, 195309 (2012).

[37] P. Le Jeune, D. Robart, X. Marie, T. Amand, M. Brousseau, J. Barrau, V. Kalevich, and D. Rodichev, Semicond. Sci. Technol. **12**, 380 (1997).

[38] A. Malinowski and R. T Harley, Phys. Rev. B **62**, 2051 (2000).